

Microstructures and Mechanical Properties of a Commercial Pure Zirconium during Rolling and Annealing at Different Temperatures

Xin Chen, Weijun He,* Wenhuan Chen, and Qing Liu

Rolling and annealing are important processes for the fabrication of zirconium alloy sheets. Herein, the microstructure and mechanical properties of a commercial pure zirconium during rolling and annealing at different temperatures are investigated. Compared with rolling at room temperature (RT), liquid nitrogen temperature (LNT) rolling will cause more inhomogeneous deformation and higher dislocation density, which significantly influences the subsequent annealing. For a given rolling reduction, the higher dislocation density in the LNT-rolled specimen causes faster recovery and recrystallization and leads to larger average grain size in subsequent annealing compared with that in the RT-rolled specimen. The inhomogeneous grain size may be attributed to the nonuniform deformation in the LNT rolling. Compared with RT rolling, higher yield strength is obtained in the LNT-rolled specimen, which is caused by the suppression of dynamic recovery in low-temperature deformation. With higher strength, the elongation of the LNT-rolled specimen is not lower than that in the RT-rolled specimen, which may be related to the inhomogeneous microstructure-induced extra work-hardening capability.

1. Introduction

Zirconium (Zr) alloys have been widely applied in nuclear reactors due to their low probability of neutron capture, acceptable mechanical properties, and excellent corrosion resistance.^[1–6] Zirconium alloys are commonly used as cladding tubes, fixed grids, or channel box in reactors.^[2,3,6] The fabrication of Zr alloys components generally includes vacuum consumable melting, forging, extrusion, hot and cold rolling, recrystallization or stress relief annealing and so on.^[7] Rolling and subsequent annealing are frequently used in the Zr alloy sheet and tube production,


which actually determine the microstructure and texture,^[7–10] thus playing a decisive role for the corrosion resistance,^[11–14] creep resistance^[15–17] and mechanical properties^[18–20] of Zr alloys.

Annealing can reduce the residual stress, recover the plastic deformation ability and tailor the grain size and texture, which plays a vital role in the Zr alloy fabrication. A special parameter was thus proposed to evaluate the effect of annealing.^[21] The microstructure and the texture evolution during annealing are not only significantly affected by annealing condition, for example temperature^[22,23] and holding time,^[8,24] but also by the pre-annealing deformation.^[6,25] Indeed, many research results on deformation and subsequent annealing in Zr alloys have been reported. Chen et al.^[7] reported that the 30% rolling reduction combined with annealing at 580 °C for 12 h imparted a superior plasticity to the Zr alloy. Kumara et al.^[26] investi-

gated the three stage of annealing in a moderately deformed Zr-4 alloy. They found that the changes in the misorientations, and corresponding rearrangements of dislocations, were the most efficient means of stress relief in Zr-4 alloy. Prakash et al.^[27] investigated the microstructural and textural evolution of ZIRLO alloy during hot rolling at different temperatures. Their results show that the slip, twinning, and recrystallization played a role in the microstructure development during hot rolling. They also contributed to the texture development, lamellae break-up, and the formation of a bimodal microstructure. Jiang et al.^[28] studied the effects of cold-rolling reduction, annealing temperature, and time on recrystallization behavior and kinetics of cold-rolled Zr-1Sn-0.3Nb-0.3Fe-0.1Cr alloy and found that the rate of the recrystallization increased with increasing annealing temperature and rolling reduction. Recrystallized grains nucleated preferentially at sites with high-density dislocation and deformation stored energy. Zhang et al.^[29] studied the microstructure evolution and mechanical properties of Zr_{98.2}Cr_{1.8} during hot rolling, solution and aging treatment (STA). It was found the bimodal microstructure was the key factor to achieve high strength (ultimate tensile strength 818 MPa) and excellent ductility (18.4%) after STA at 750 °C. Gerspach et al.^[30] investigated the texture stability during primary recrystallization of cold-rolled Zr702 alloy and found that a small strain favored an orientation-dependent nucleation and a strong deformed

Dr. X. Chen, Prof. W. He, Dr. W. Chen, Prof. Q. Liu
College of Materials Science and Engineering
Chongqing University
Chongqing 400044, P. R. China
E-mail: weijun.he@cqu.edu.cn

Prof. W. He
International Joint Laboratory for Light Alloys (Ministry of Education),
College of Materials Science and Engineering
Chongqing University
Chongqing 400044, P. R. China

 The ORCID identification number(s) for the author(s) of this article can be found under <https://doi.org/10.1002/adem.202001039>.

DOI: 10.1002/adem.202001039

texture may promote the orientation-dependent grain growth. Guo et al.^[31] found an enhancement of strength in a severe cryo-rolled Zr alloy, which was mainly caused by the high density of dislocation.

As result of the hexagonal close-packed (HCP) structure, the easy-to-activate independent slip system in Zr alloy is limited at room temperature (RT), which gets better with the increase in deformation temperature. It was reported that the deformation mechanism, for example the activation of slip systems, during rolling at high temperature was different from that at RT,^[32] which may cause different deformed microstructure, thus affecting the microstructure and texture evolution in the subsequent annealing. Actually, when deformed at low temperature, for example at liquid nitrogen temperature (LNT), the deformation mechanism may be different from that at RT, thus leading to different annealing behavior. However, the effect of low-temperature deformation on the subsequent annealing behavior was rarely investigated in Zr alloys.

In this work, the microstructures and mechanical properties of a commercial pure Zr rolled and annealed at RT and LNT are investigated. The microstructures were characterized by electron backscatter diffraction (EBSD). Uniaxial tension and compression are performed to evaluate the mechanical properties. The underlying deformation and annealing mechanisms are discussed. The motivation of this work is to explore the effect of low-temperature deformation on the microstructure and mechanical properties in zirconium alloys.

2. Experimental Section

Commercial pure Zr plate (Zr702), with 4.4 mm thickness, was used in the current work. The as-received plate was composed of fully recrystallized microstructure. The initial average grain size was $\approx 11.9 \mu\text{m}$, which was obtained by grain size statistics of Channel5 software. Grains were uniform and equiaxed, as shown in Figure 1a. The initial texture of the as-received plate was a typical basal texture,^[8] as shown in Figure 1b. The distribution of the misorientation angle is presented in Figure 1c. The distribution peak appears at $\approx 30^\circ$, which is a common distribution in recrystallized Zr alloys.^[7,28]

To perform rolling, small plates with dimension of 40 mm (rolling direction [RD]) \times 20 mm (transverse direction [TD]) were cut from the as-received plate. Rolling was carried out at RT and

LNT. Two reduction levels, 15% and 30%, were applied at each rolling temperature. The RD was along the original RD of the as-received plate. During rolling, 15% per pass was used. For the rolling at LNT, before each rolling pass, the small plate was immersed in liquid nitrogen for 30 min to ensure that the sample was sufficiently cooled. After rolling deformation, small specimens with dimension of 5 mm \times 4 mm (RD \times TD) were cut from the rolled plates to conduct annealing. The small specimens were annealed at 600, 650, and 700 $^\circ\text{C}$ for 30 min. The annealing process was carried out in vacuum furnace.

For microstructure characterization, sample surface was carefully grinded. Electrolytic polishing was adapted to obtain smooth and stress-free fresh surface. An MIR3 TESCAN field scanning electron microscope equipped with an EBSD probe was used to carry the microstructure characterization. The experimental voltage was 20 kV, and the working distance was 15 mm. HKL system was used to capture EBSD information. The obtained EBSD data was processed by Channel5 software.

For mechanical property testing, uniaxial tension and compression were performed at RT. Tension was carried out for the as-received and the rolled plates, whereas compression was conducted to the as-received, the rolled, and the annealed samples. Specimens for uniaxial tensile tests were prepared with the gauge area of 12 mm \times 6 mm (RD \times TD). Same specimen size as that for the annealing was used in the compression test. The loading direction was along the RD. Static loading, with strain rate $\approx 10^{-2} \text{ s}$, was used. The tension and compression were tested on a SHIMADZU AG-X 50KN machine.

To facilitate the later analysis, the specimens were named after the rolling and the annealing history. For example, LNT-30%-700 represents that the specimen was annealed at 700 $^\circ\text{C}$ for 30 min after 30% rolling at LNT.

3. Results

3.1. Microstructure After Rolling Deformation

The orientation imaging maps with inverse pole figure (IPF) coloring (IPF maps) of the specimens rolled at RT and LNT are shown in Figure 2. In the IPF map, high-angle grain boundary (misorientation angle $> 10^\circ$) and low angle grain boundary (sub-grain boundaries, $2^\circ < \text{misorientation angle} < 10^\circ$) are represented by dark coarse line and gray fine line, respectively.

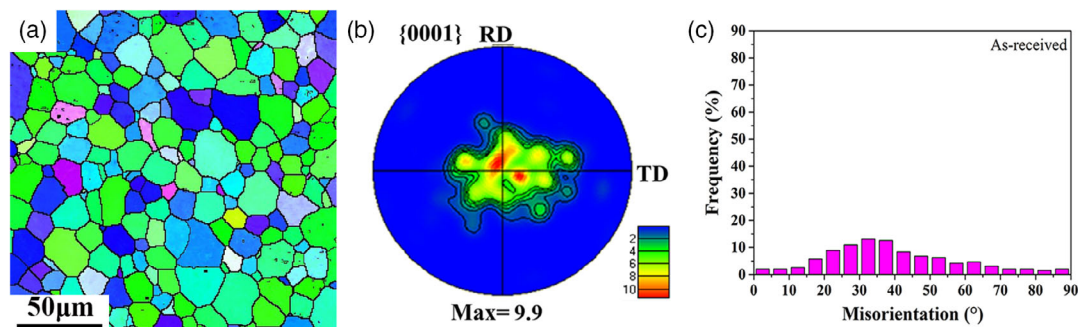


Figure 1. Initial microstructure of the as-received material: a) orientation imaging map, which is also denoted as IPF map, b) {0001} pole figure, and c) misorientation angle distribution.

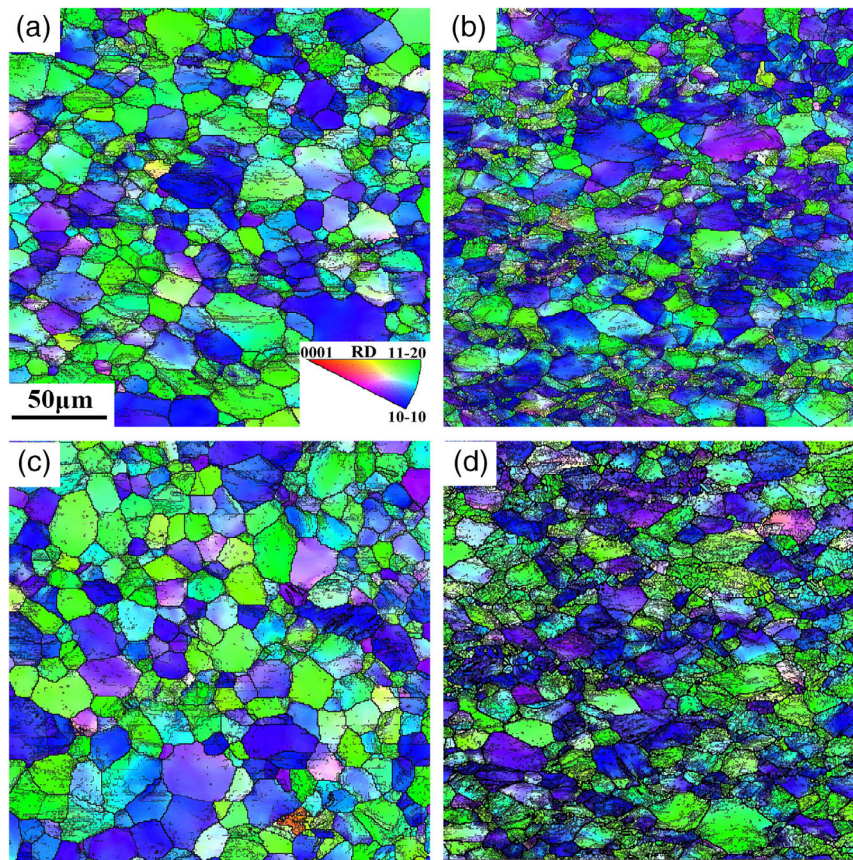


Figure 2. IPF maps of deformed samples: a) RT-15%, b) RT-30%, c) LNT-15%, d) LNT-30%.

The grains are elongated after rolling, especially at large rolling reduction (30%). Compared with the low degree of rolling (15%), more low-angle grain boundaries are observed in the specimen with large rolling reduction (30%). The LNT rolling is supposed to show higher residual dislocation density, thus more low-angle grain boundaries compared with the RT rolling as dynamic recovery is hindered when rolling at LNT.^[33,34] However, based on the IPF map, no clear difference can be noted between the RT and LNT sample at a given rolling reduction. In addition, no twin lamellar is found in the LNT-rolled specimen as well as in the RT-rolled specimen, which is different from the report in the literature.^[33] The low strain rate used in the rolling process and the fine initial grain size may be not beneficial for the activation of twinning.

To further compare the microstructure deformed at different temperatures, the correlated misorientation angle was counted and presented in **Figure 3**. Compared with the misorientation angle distribution of the as-received sample (Figure 1c), the frequency of the low-angle boundary (2° – 10°) are significantly increased after rolling deformation. The frequency of the low-angle boundary increases with the increase in the applied rolling reduction. In addition, for a given rolling reduction (15% or 30%), the frequency of the low-angle boundary in the sample rolled at LNT is higher than that in the sample rolled at RT. Higher frequency of the low-angle boundary may imply higher stored dislocation density and deformation storage

energy, which agrees with the general expectation that low-temperature deformation can hinder the dynamic recovery.^[34,35]

3.2. Microstructure After Annealing at Different Temperatures

The IPF maps of specimens after annealing at different temperatures are shown in **Figure 4, 5**. It indicates that many grains are still elongated and many sub-grain boundaries are visible when annealing at low temperature (600°C) despite the strain level and the pre-annealing deformation temperature. This implies that recrystallization is not finished when annealing at 600°C for 30 min. Recovery may be the main mechanism for this low-temperature annealing. With the increase in the annealing temperature, the degree of the recrystallization is higher and higher. When annealing at 700°C for 30 min, complete recrystallization may occur as majority of the grains show equiaxed profile and are free from sub-grain boundaries. For a given rolling-reduction, the annealed microstructure between the LNT and the RT-rolled sample show no clear difference when annealing at 600 and 650°C . However, it is worth to note that there are many larger grains in the LNT-rolled sample compared with that in the RT-rolled sample after recrystallization annealing (700°C), especially in sample with small rolling reduction, as marked with red circles in Figure 4f. This implies that the grain size is more inhomogeneous after the annealing of LNT-rolled sample.

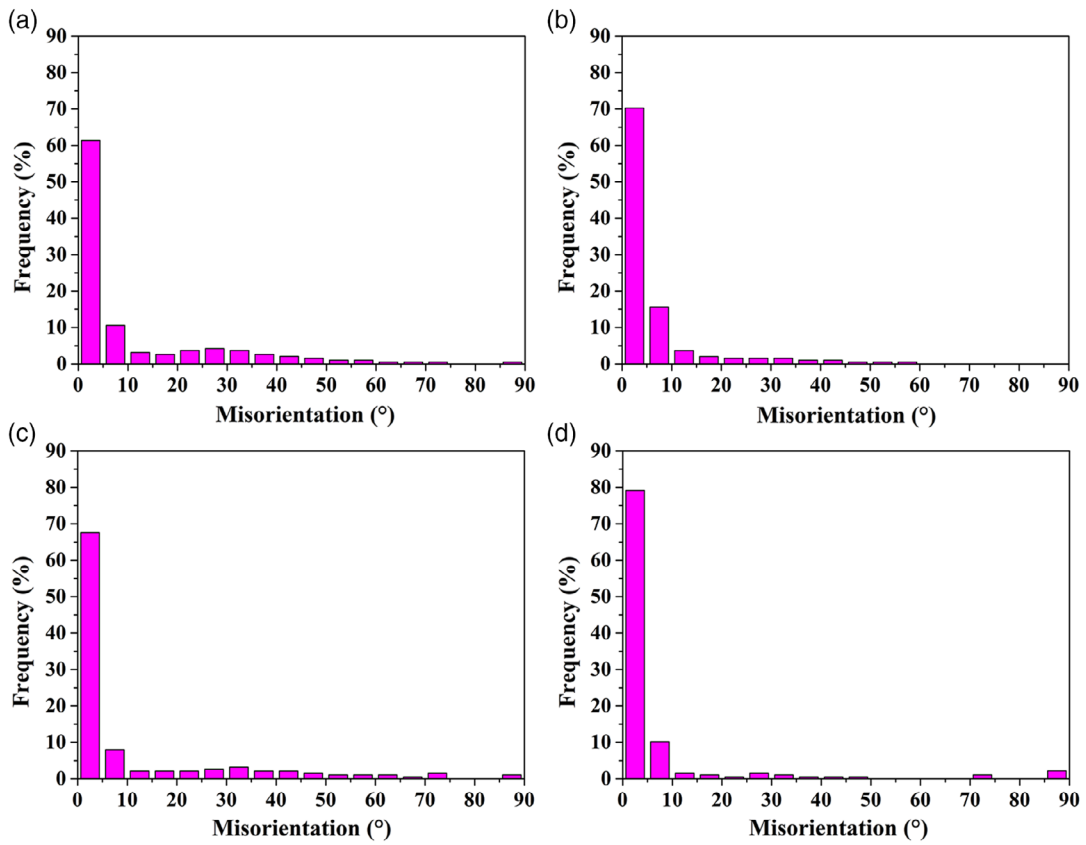


Figure 3. Distribution of misorientation angle of deformed samples: a) RT-15%, b) RT-30%, c) LNT-15%, d) LNT-30%.

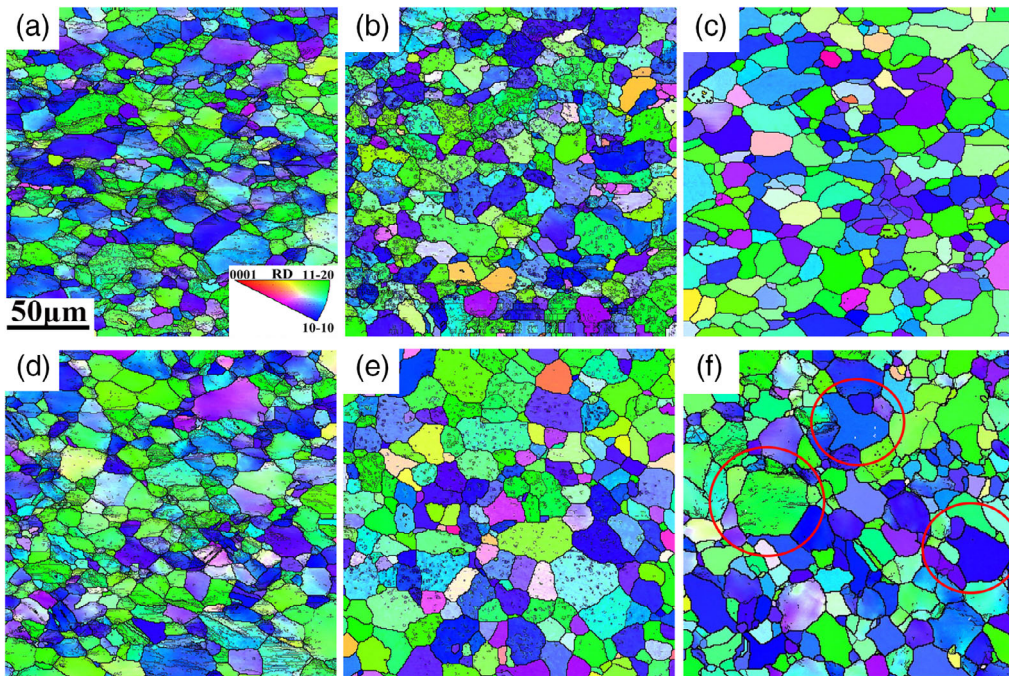


Figure 4. IPF maps of 15% rolled sample after annealing: a) RT-15%-600, b) RT-15%-650, c) RT-15%-700, d) LNT-15%-600, e) LNT-15%-650, and f) LNT-15%-700.

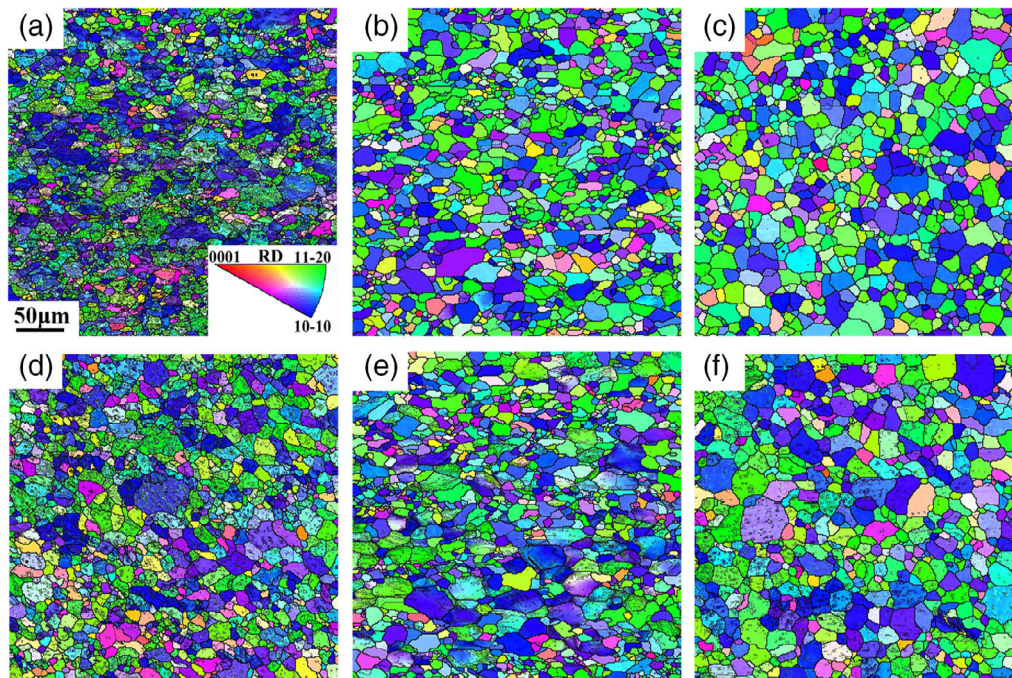


Figure 5. IPF maps of 30% rolled sample after annealing: a) RT-30%-600, b) RT-30%-650, c) RT-30%-700, d) LNT-30%-600, e) LNT-30%-650, and f) LNT-30%-700.

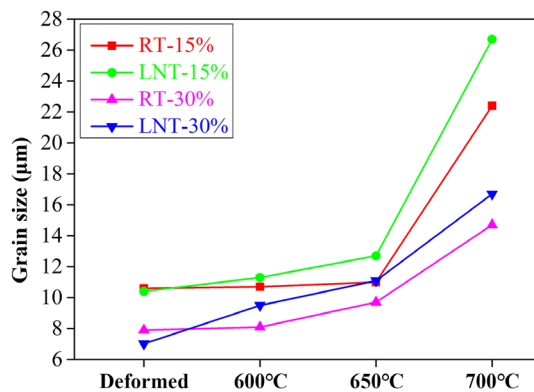


Figure 6. Average grain size for the rolled and the annealed samples.

To quantitatively analyze the evolution of the grain size, the linear intercept method was used to measure the average grain size of specimen in each state. The results are shown in **Figure 6**. The average grain size in the original state is 11.9 µm. After rolling deformation, the grain size has decreased. The average grain size of RT-15%, LNT-15%, RT-30%, and LNT-30% is 10.6, 10.4, 7.9, and 7.1 µm, respectively. The decrease in the average grain size during rolling is because that the grains are elongated along the RD but squashed along the normal direction. The lines used in the linear intercept method are mainly parallel to the normal direction. After annealing, the average grain size increases. However, the amplitude of the increase after annealing at 600 and 650 °C is relatively smaller. After annealing at 700 °C, the average grain size significantly increases compared with the rolled specimens. The average grain size of RT-15%-700,

LNT-15%-700, RT-30%-700, and LNT-30%-700 is 22.8, 26.7, and 14.7 µm, respectively, which is larger than the double size of that in the deformed state. The small increase in grain size for low-temperature annealing (600 and 650 °C) and large increase in grain size for high-temperature annealing (700 °C) agree well with the observed results from IPF maps.

For a given rolling reduction and annealing temperature, the average grain size of the LNT-rolled specimen is larger than that in the RT-rolled specimen after annealing, especially after 700 °C annealing. **Figure 7** shows the statistics of the grain size distribution after annealing at 700 °C for 30 min. The grain size distribution of the LNT-rolled samples has a wider range than that in the RT-rolled sample. This demonstrates that the recrystallized grain size of the specimen rolled at LNT is more inhomogeneous compared with RT-rolled sample. The larger average annealed grain size and the inhomogeneous grain size distribution in the LNT-rolled sample may be attributed to the special deformed microstructure when rolling at low (LNT) temperature, which will be further discussed in Section 4. In addition, for a given rolling reduction, **Figure 6** indicates that the average grain size of the LNT-rolled specimen start to increase at lower annealing temperature compared with RT-rolled sample, which may be caused by the relative higher storage deformation energy when rolling at lower temperature (**Figure 3**).

3.3. Mechanical Properties After Deformation and Annealing

Figure 8 shows the tensile and the compressive strain–stress curves of the as-received and the rolled specimens. Yield strengths and tensile fracture elongations are listed in **Table 1**. **Figure 8a** indicates that the yield strength significantly increases

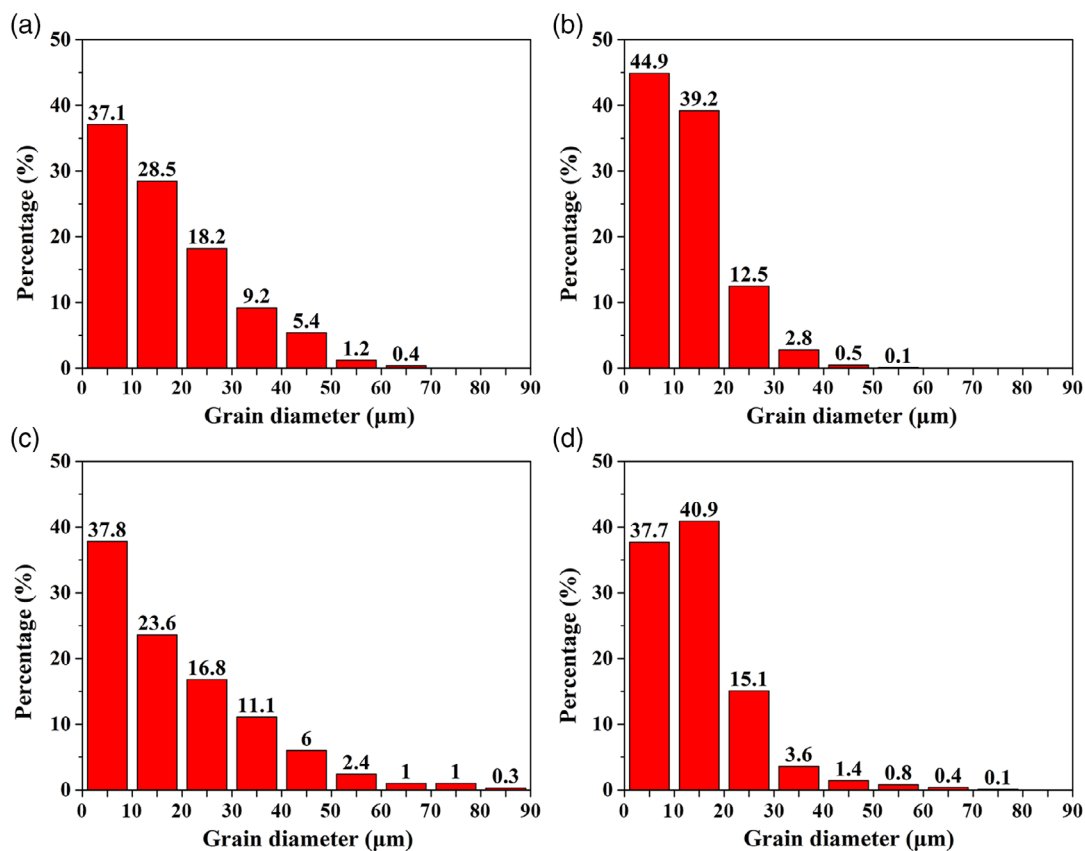


Figure 7. Distribution of grain size after annealing at 700 °C for 30 min: a) RT-15%-700, b) RT-30%-700, c) LNT-15%-700, d) LNT-30%-700.

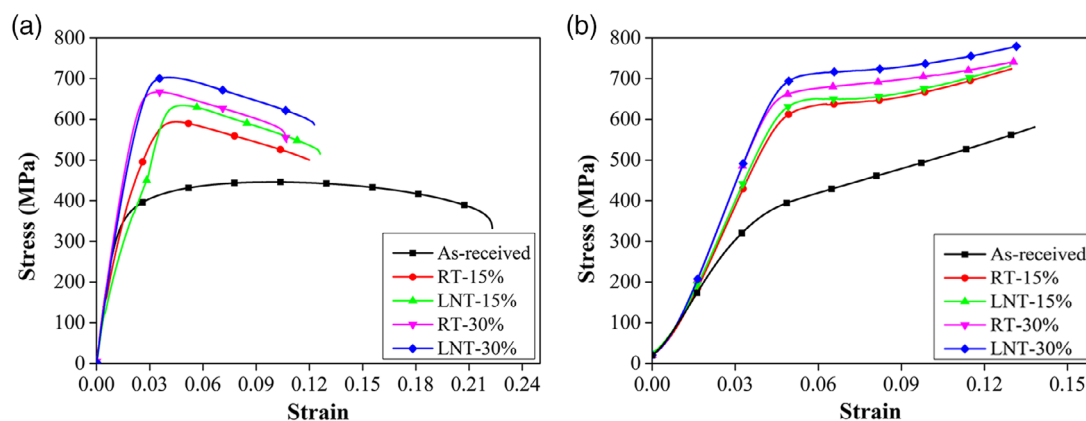


Figure 8. Strain–stress curves of the as-received and deformed specimens: a) tension along the RD and b) compression along the RD.

after rolling due to work hardening, whereas the tensile fracture elongation clearly decreases (from $\approx 22\%$ to $\approx 10\%$). For a given rolling temperature, the larger the applied rolling reduction, the higher the yield strength and the lower the tensile fracture elongation are. This agrees well with the often observed trade-off phenomenon between strength and ductility in many metals. For a given rolling reduction, the LNT-rolled specimens show higher yield strength than that of the RT-rolled specimen. As mentioned on Section 3.1, compared with RT rolling, the dynamic recovery was suppressed to a greater extent when rolled

at lower temperature (LNT),^[31,34,35] which leads to a higher dislocation density, thus causing the higher degree of work hardening. However, it is worth to note that although with higher strength, the elongation of the LNT-rolled specimens are not lower than that of the RT-rolled specimens. The synergistic strengthening and toughening in LNT-rolled specimens may be attributed to the special inhomogeneous microstructure. It is worth to note that the inhomogeneous microstructure mentioned in this work is not the uneven distribution of grain size. The inhomogeneous structure in the current work is mainly

Table 1. Yield strength and tensile fracture elongation of the as-received and deformed specimens.

Specimens	Yield strength [MPa]		Fracture elongation [%]
	Tension	Compression	
As-received	361	342	22.2
RT-15%	583	621	12.1
LNT-15%	637	643	12.8
RT-30%	661	667	10.6
LNT-30%	708	718	12.3

formed by the grains with different degrees of deformation in LNT rolling, which further causes to the inhomogeneous mechanical property among grains, thus leading to hetero-deformation in tension.^[36] In fact, similar results have been observed in electroplastic rolling (EPR) and RT rolling high-purity Zr sheet,^[37,38] in which the hetero-structured zirconium alloy exhibited a combination of high strength and good ductility. The author believed that it was caused by the back-stress strengthening and hardening of the heterogeneous structure. In addition, many investigations found that inhomogeneous microstructure may provide extra strengthening and work hardening capability in other metallic materials.^[39,40] However, much further work need be done to verify the LNT-rolling-induced synergistic strengthening and toughening and reveal the underlying mechanisms.

Figure 8b shows that the compressive strength follows similar tendency as the tensile strength. For a given rolling temperature, the larger the applied strain level, the higher the compressive

strength is. For a given rolling reduction, the LNT-rolled specimen shows a higher compressive strength than that of the RT-rolled specimen. When comparing the tensile strength and the compressive strength of same specimen, asymmetric yielding phenomenon can be found. For the as-received sample, the compressive yield strength (342 MPa) is lower than the tensile yield strength (361 MPa), which may be attributed to the activation of twinning. In zirconium alloys, it was reported that the RT critical resolved shear stress (CRSS) of deformation systems follow the order: prismatic slip < {10–12} tensile twins < pyramidal slip.^[41–43] When compressing along the RD, it is easy to activate the prismatic slip and {10–12} tensile twinning as a result of the basal texture.^[43,44] When tension along the RD, the original texture is not conducive to the generation of tensile twins. Prismatic slip and pyramidal slip may be activated to accommodate the deformation. As the CRSS of pyramidal slip is higher than that of {10–12} tensile twinning, the tensile yield strength is higher than the compressive yield strength.

After rolling deformation, the tensile yield strength is lower than the compressive yield strength, which is opposite to the tendency in the as-received specimen. After rolling, the average grain sizes are reduced, which may increase the CRSS of the tensile twinning as the activation of twinning was reported to be very size sensitive.^[45,46] In addition, many sub-grain boundaries are appeared, which may also contribute to the increase in the CRSS of the tensile twinning. The activation of tensile twinning with high CRSS may cause the higher compressive yield strength. Moreover, the tension along the RD has similar deformation path as the rolling, whereas the compression along the RD significantly violates the rolling deformation path. Strain path change was reported to cause hardening,^[47,48] which may contribute to the higher compressive yield strength.

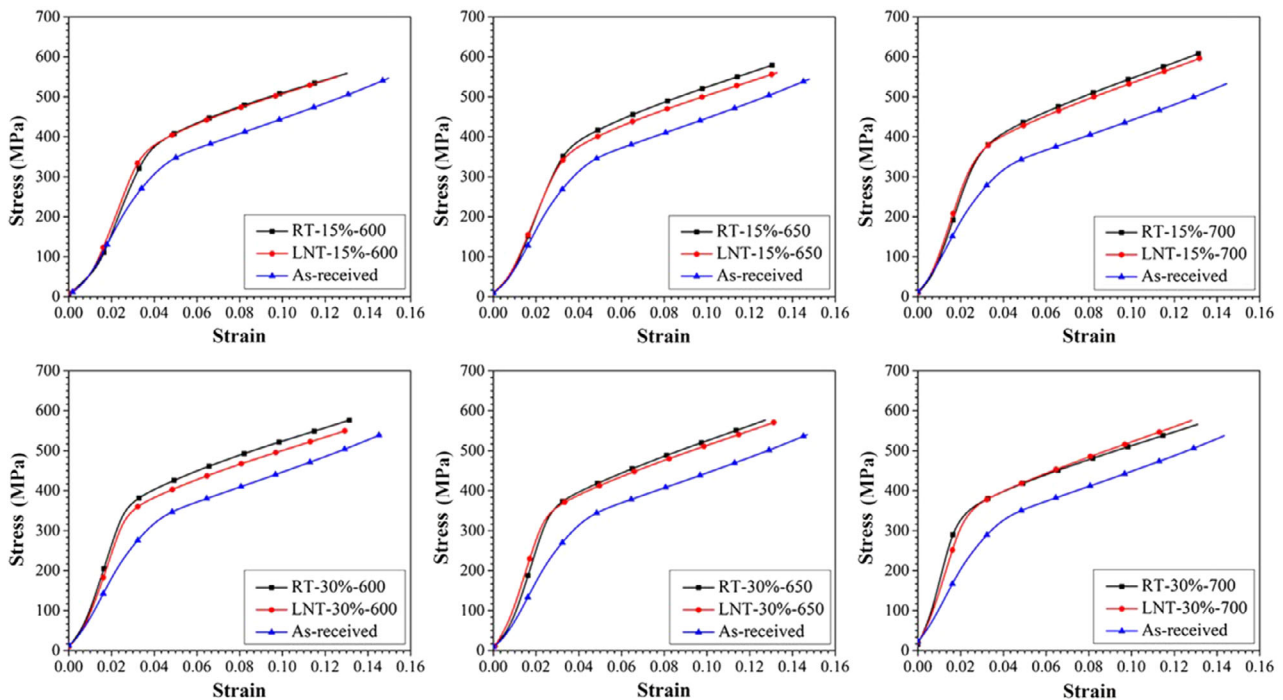


Figure 9. Strain–stress curves of as-received and annealed specimens when compression along the RD.

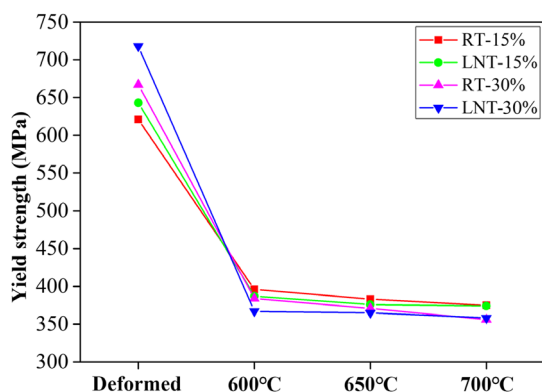


Figure 10. Yield strength of the deformed and annealed samples when compression along the RD.

Compressive stress–strain curves of the annealed specimens are shown in **Figure 9**. For comparison, the stress–strain curve of the as-received specimen is also repeated in **Figure 9**. Compressive yield strengths of the as-received, deformed, and the annealed specimens are shown in **Figure 10**. It can be found that the yield strength is clearly reduced after annealing despite the applied rolling reduction, the rolling temperature, and the annealing temperature. As shown in **Figure 4** and **5**, the recrystallization is not completed when annealing at low temperature (600 and 650 °C). Therefore, the significant decrease in the yield strength should mainly be caused by the recovery. The high stacking fault energy of Zr makes recovery easy to happen,^[49,50] thus leading to the rapid decrease in strength. After annealing at 600 and 650 °C, the LNT-rolled specimens show a little lower strength than that of the RT-rolled sample for a given rolling reduction, which may be caused by the higher storage deformation energy induced fast recovery and recrystallization.

4. Discussion

4.1. Effect of Rolling Temperature on the Deformation Mechanism

In theory, the deformation mechanism of Zr alloy will change with the increase or decrease in deformation temperature, which may form different deformed microstructure, thus affecting subsequent annealing. In the current study, the misorientation angle distribution (**Figure 3**) indicates that the frequency of the low-angle grain boundary is higher in the LNT-rolled specimen compared to that in the RT-rolled specimen. In addition, the average grain size in the annealed specimen with rolling at LNT is larger than that in the specimen rolled in the RT (**Figure 6** and **7**). The recovery and recrystallization are closely related to the deformed microstructure. Different annealed grain sizes imply that the deformed microstructures are different between the LNT and RT specimen. Moreover, compared with the RT-rolled specimen, higher strength is achieved without losing of elongation in the LNT-rolled specimen, which also implies that the LNT-deformed microstructure is different from the RT-deformed microstructure.

To further reveal the difference between LNT-rolled specimen and RT-rolled specimen, average orientation difference inside grain is calculated for the as-received and the rolled specimens, as shown in **Figure 11**. The blue, red, and yellow part represents the recrystallization, deformation and substructure region, respectively. Areas with average orientation difference inside grain larger than α are classified as deformed areas. Some areas are composed of sub-grains. The overall average orientation difference inside grain is smaller than α , but the average orientation difference inside grain among sub-grains is larger than α . Such areas are classified as substructures. Areas with the overall average orientation difference inside grain smaller than α are classified as recrystallization. The default value is $\alpha = 7^\circ$. It can be observed from **Figure 11a** that the as-received sheet is mainly composed of recrystallized regions. After rolling with 15% reduction, the RT-rolled specimen is mainly composed of deformation microstructure and substructure. In the LNT-rolled specimen, it is also composed with substructure and deformed microstructure. However, obviously more substructure can be found in the LNT-rolled specimen. This demonstrates that the deformation in the LNT-rolled sample (15%) is more inhomogeneous.

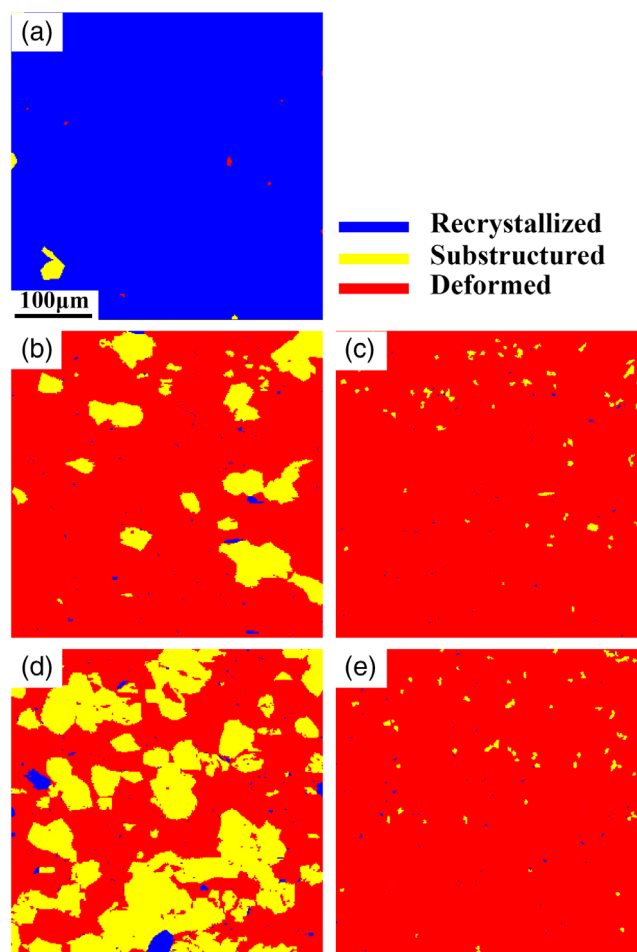


Figure 11. Distribution of average orientation difference inside grain in the as-received and deformed samples: a) As-received, b) RT-15%, c) RT-30%, d) LNT-15%, e) LNT-30%.

The inhomogeneous deformation during LNT rolling may be attributed to the evolution of CRSS of deformation mode with the temperature. In zirconium alloys, the most common slip modes are prismatic slip and pyramidal slip.^[51,52] During rolling deformation, both prismatic slip and pyramidal slip need to be activated to accommodate the rolling deformation as no twins were found in this work. It was reported that CRSS increased with the decreasing deformation temperature.^[53] Compared with deformation at RT, the difference between the CRSS of the prismatic slip and the pyramidal slip has been enlarged when rolling at LNT. According to the Schmid formula, the activation of a slip system depends on the orientation and the CRSS. For slip mode with a higher CRSS, the slip is harder to activate and more sensitive to the orientation. Therefore, in the LNT rolling, the deformation of a grain is more sensitive to the initial crystal

orientation compared with that in the RT rolling. Deformation will only occur in a more favorable orientation in the LNT, which cause the more inhomogeneous deformation. As the rolling deformation increases to 30%, the effect of temperature on the deformation uniformity decreases. It can be seen that most of the grains belong to deformed microstructure. This is because this rolling deformation is large enough to make majority grains take part in the deformation.

4.2. Effect of Rolling Process on Recrystallized Grain Size

As mentioned in Section 3.2, the recrystallized grain size in the specimen with pre-annealing deformation at LNT is larger than that at RT, especially in the LNT-15%-700 specimen. The larger average grain size may be caused by the higher deformation

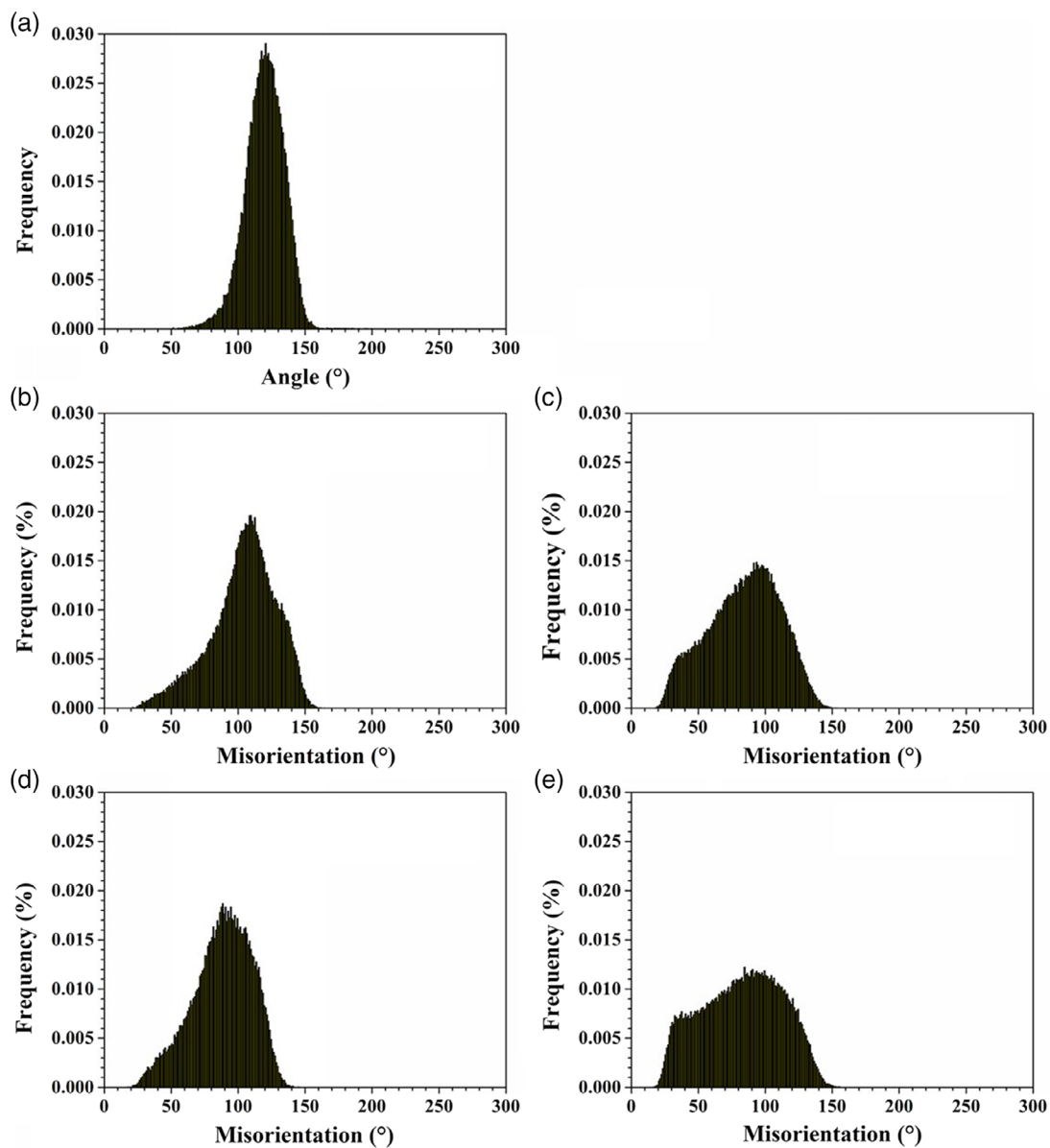


Figure 12. BC value in the as-received and deformed samples: a) As-received, b) RT-15%, c) RT-30%, d) LNT-15%, e) LNT-30%.

energy storage in the LNT-rolled specimen. According to the proportion of low angle of grain boundaries (Figure 3), it is assumed that the order of deformation storage energy is: LNT-30% > RT-30% > LNT-15% > RT-15%. To further confirm this, the band contrast (BC) values in different rolled specimens were counted, as shown in Figure 12. The BC value can reflect the quality of the EBSD image. In general, when the deformation is severe, the dislocation density is high, thus leading to serious lattice distortion. The resulting image quality will be poor. Therefore, the BC value at this condition will be lower. In this way, the BC value can reflect the deformation storage energy to some degree. The lower the BC value, the higher the storage energy is. Figure 12 indicates that the order of the deformation energy storage is LNT-30% > RT-30% > LNT-15% > RT-15% > as-received, which agrees well with the result based on low angle of grain boundary.

The process of recrystallization is divided into nucleation and growth. Deformation storage energy is the driving source for the nucleation and growth. The grain size is determined by the nucleation rate and the migration speed of high-angle grain boundaries (grain growth).^[54,55] A smaller nucleation rate and a larger grain boundary migration speed will result in a larger grain size. In the current study, for a given rolling reduction, the nucleation rate during annealing may be very similar between the LNT and RT-rolled specimen. With higher deformation energy storage, the grain growth is relatively higher, thus leading to the larger average grain size in the LNT-rolled specimen. For a given deformation temperature, higher rolling reduction (30%) may lead to higher nucleation rate, which causes the finer annealed grain size.

In addition, except for the larger average grain size, the recrystallized grain size in the specimen with pre-annealing deformation at LNT is not uniform, where some abnormally large grains exist, especially in the LNT-15%-700 specimen (Figure 4f). The nonuniform recrystallized grain size in the LNT-rolled specimen may be attributed to the inhomogeneous deformation. During annealing treatment of Zr-2Hf with 55% plane strain compression deformation, Zhu et al.^[56] found that merging small sub-grains to form large size sub-grains was one of the main nucleation mechanism. Jedrychowski et al.^[57] reported that for

a moderate deformed zirconium alloy, strain-induced grain boundary migration (SIBM) is the primary way of grain growth. In the current study, more substructure regions, which are composed of sub-grains, are formed in the LNT-15% sample. These sub-grains themselves or after merging with other sub-grains can be the nucleation cores during annealing, which is followed by SIBM. As a result of inhomogeneous deformation in the LNT-15% specimen, some grains, which are surrounded by severely deformed regions, grow faster than other grains, thus leading to the nonuniform grain size, as schematically shown in Figure 13.

5. Conclusion

In this work, Zr702 plate was rolled at RT and LNT, which were followed by annealing at different temperatures. Microstructure and texture evolution during deformation and annealing were examined by EBSD. The mechanical properties after rolling and annealing were investigated by uniaxial tension and compression. The primary conclusions can be drawn as follows: 1) For a small rolling reduction (15%), the LNT rolling deformation is more inhomogeneous than that in the RT rolling, which may be closely related to the increase in the CRSS of slip mode with decreasing deformation temperature. 2) Compared with RT rolling, higher yield strength is obtained in the LNT-rolled specimen, which is caused by the suppression of dynamic recovery and thus higher density of dislocation density in low-temperature deformation. With higher strength, the tensile elongation of the LNT-rolled specimen is not lower than that in the RT-rolled specimen, which may be related to the inhomogeneous deformation microstructure induced extra work-hardening capability. 3) For a given rolling reduction, compared with the RT rolling, the higher deformation energy storage in the LNT-rolled specimen causes faster recovery and recrystallization and leads to larger average annealed grain size in subsequent annealing. Inhomogeneous recrystallized grain size is formed in the sample rolled at LNT and annealing at 700 °C, especially at 15% rolling reduction, which may be attributed the nonuniform deformation in the LNT rolling.

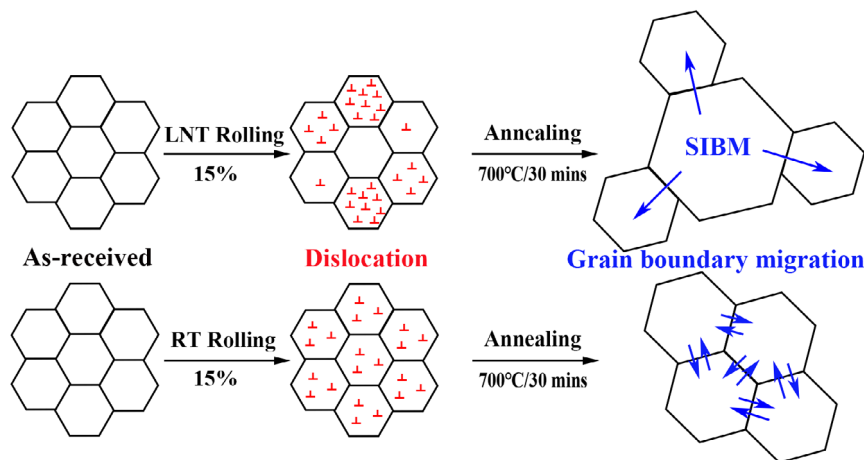


Figure 13. Schematic illustration on the formation of nonuniform grain size in the LNT-rolled specimen.

Acknowledgements

The authors express their sincere thanks for the financial support from the National Natural Science Foundation of China (Projects 51971041, 51601023, and 51421001) and Natural Science Foundation of Chongqing (Projects no. cstc2019jcyj-msxmX0234).

Conflict of Interest

The authors declare no conflict of interest.

Keywords

liquid-nitrogen-temperature rolling, low-temperature deformation, mechanical properties, recrystallization, Zr alloys

Received: September 2, 2020

Revised: October 19, 2020

Published online:

-
- [1] S. J. Zinkle, G. S. Was, *Acta Mater.* **2013**, *61*, 735.
 [2] S. Banerjee, M. K. Banerjee, *Ref. Mod. Mater. Sci. Mater. Eng.* **2016**, *34*, 6287.
 [3] V. Kalavathi, R. K. Bhuyan, *Mater. Today Proc.* **2019**, *19*, 781.
 [4] K. L. Murty, I. Charit, *Prog. Nucl. Eng.* **2006**, *48*, 325.
 [5] G. C. Kaschner, C. N. Tome, I. J. Beyerlein, S. C. Vogel, D. Brown, R. J. McCabe, *Acta Mater.* **2006**, *54*, 2887.
 [6] L. J. Chai, B. F. Luan, K. L. Murty, Q. Liu, *Acta Mater.* **2013**, *61*, 3099.
 [7] J. Chen, Y. L. Jiang, H. Q. Liu, D. Q. Yi, R. Q. Zhang, X. Dai, S. Q. Liu, *J. Nucl. Mater.* **2019**, *524*, 226.
 [8] W. J. He, X. Chen, N. Liu, B. F. Luan, G. H. Yuan, Q. Liu, *J. Alloys Compd.* **2017**, *699*, 160.
 [9] S. X. Liang, M. Z. Ma, R. Jing, C. L. Tan, R. P. Liu, *Mater. Sci. Eng. A* **2012**, *541*, 67.
 [10] C. Vanithaa, M. Kiran Kumar, G. K. Dey, D. Srivastava, R. Tewari, S. Banerjee, *Mater. Sci. Eng. A* **2009**, *519*, 51.
 [11] F. Y. Zhou, B. L. Wang, K. J. Qiu, W. J. Lin, L. Li, Y. B. Wang, F. L. Nie, Y. F. Zheng, *Mater. Sci. Eng. C* **2012**, *32*, 851.
 [12] T. L. Yau, *Shreir's Corros.* **2016**, *3*, 2094.
 [13] M. Y. Yao, Y. F. Shen, Q. Li, J. C. Peng, B. X. Zhou, J. L. Zhang, *J. Nucl. Mater.* **2013**, *435*, 63.
 [14] S. Xie, B. Zhou, X. Liang, W. Liu, H. Li, Q. Li, M. Yao, J. Zhang, *Corros. Sci.* **2017**, *126*, 44.
 [15] J. Y. Kim, K. S. Na, Y. D. Kim, J. H. Kim, K. Y. Lee, K. N. Kim, S. J. Kim, *Acta Mech. Solida Sinica* **2008**, *21*, 308.
 [16] W. Li, R. A. Holt, *J. Nucl. Mater.* **2010**, *401*, 25.
 [17] W. Li, R. A. Holt, M. R. Daymond, F. Xu, *J. Nucl. Mater.* **2011**, *412*, 138.
 [18] Z. G. Zhang, Z. H. Feng, X. J. Jiang, X. Y. Zhang, M. Z. Ma, R. P. Liu, *Mater. Sci. Eng. A* **2016**, *652*, 77.
 [19] X. Zhang, B. Zhang, S. G. Liu, C. Q. Xia, X. Y. Zhang, M. Z. Ma, R. P. Liu, *Mater. Sci. Eng. A* **2020**, *773*, 723.
 [20] R. Kondo, N. Nomura, X. Suyalatu, Y. Tsutsumi, H. Doi, T. Hanawa, *Acta Biomater.* **7**, **2011**, 4278.
 [21] J. D. Roboson, *J. Nucl. Mater.* **2019**, *527*, 151814.
 [22] Z. N. Yang, X. B. Wang, F. Liu, F. C. Zhang, L. J. Chai, R. S. Qiu, L. Y. Chen, *J. Alloys Compd.* **2019**, *776*, 242.
 [23] W. J. He, J. T. Ma, Y. X. Zhang, H. Y. Wen, Q. Liu, *Mater. Sci. and Eng. A* **2018**, *713*, 214.
 [24] H. K. Zeytin, C. Kubilay, H. Aydin, *Mater. Lett.* **2008**, *62*, 2651.
 [25] Y. Wang, W. J. He, N. Liu, *AdrienChapuis. Mater. Character.* **2018**, *136*, 1.
 [26] G. Kumara, R. Singh, J. Singh, D. Srivastava, G. K. Dey, I. Samajdar, *J. Nucl. Mater.* **2015**, *466*, 243.
 [27] D. G. Leo Prakash, M. Preuss, M. Dahlback, J. Quinta da Fonseca, *Acta Mater.* **2015**, *88*, 389.
 [28] Y. L. Jiang, H. Q. Liu, D. Q. Yi, G. Y. Lin, X. Da, R. Q. Zhang, Y. D. Sun, S. Q. Liu, *Trans. Nonferrous Metals Soc. China* **2018**, *28*, 651.
 [29] Z. G. Zhang, Y. K. Zhou, X. J. Jiang, Z. H. Feng, C. Q. Xia, X. Y. Zhang, M. Z. Ma, R. P. Liu, *Mater. Sci. Eng. A* **2016**, *651*, 370.
 [30] F. Gerspach, N. Bozzolo, F. Wagner, *Scr. Mater.* **2009**, *60*, 203.
 [31] D. F. Guo, M. Li, Y. D. Shi, Z. B. Zhang, T. Y. Ma, H. T. Zhang, X. Y. Zhang, *Mater. Sci. Eng. A* **2012**, *558*, 611.
 [32] Q. H. Zeng, B. F. Luan, X. Qiu, Q. Liu, *J. Alloys Compd.* **2019**, *30*, 318.
 [33] L. J. Chai, B. F. Luan, D. P. Xiao, M. Zhang, K. L. Murty, Q. Liu, *Mater. Des.* **2015**, *85*, 296.
 [34] V. Kumar, D. Kumar, *Mater. Sci. Eng. A* **2017**, *691*, 211.
 [35] D. Song, G. W. Wang, Z. K. Zhou, E. E. Klu, A. B. Ma, Y. N. Wu, J. P. Sun, J. H. Jiang, X. L. Ma, *Mater. Sci. Eng. A* **2020**, *773*, 138880.
 [36] Y. T. Zhu, X. L. Wu, *Mater. Res. Lett.* **2019**, *7*, 393.
 [37] M. Li, D. F. Guo, J. T. Li, S. M. Zhu, C. Xu, K. F. Li, Y. D. Zhao, B. N. Wei, Q. Zhang, X. Y. Zhang, *Mater. Sci. Eng. A* **2018**, *722*, 93.
 [38] W. K. Shan, G. S. Zhang, K. F. Li, J. Y. Hao, M. Li, Z. Gong, Y. W. Gao, D. F. Guo, *J. Alloys Compd.* **2020**, *819*, 152955.
 [39] W. H. Chen, W. J. He, Z. J. Chen, B. Jiang, Q. Liu, *Int. J. Plast.* **2020**, *133*, 102806.
 [40] H. Wu, G. H. Fan, *Proc. Mater. Sci.* **2020**, *113*, 100675.
 [41] J. W. Christian, S. Mahajan, *Prog. Mater. Sci.* **1995**, *39*, 1.
 [42] W. J. He, A. Chapuis, X. Chen, Q. Liu, *Mater. Sci. Eng. A* **2018**, *734*, 364.
 [43] J. C. Gong, T. B. Britton, M. A. Cuddihy, F. P. E. Dunne, A. J. Wilkinson, *Acta Mater.* **2015**, *96*, 249.
 [44] X. Chen, Q. H. Zeng, W. J. He, Q. Liu, *Mater. Sci. Eng. A* **2020**, *789*, 139650.
 [45] Z. W. Huang, P. L. Yong, H. Zhou, Y. S. Li, *Mater. Sci. Eng. A* **2020**, *773*, 38721.
 [46] W. J. He, X. Chen, H. Chen, Q. Liu, *Mater. Sci. Eng. A* **2018**, *724*, 576.
 [47] R. K. Verma, T. Kuwabara, K. Chung, A. Haldar, *Int. J. Plast.* **2017**, *27*, 82.
 [48] H. Haddadi, S. Bouvier, M. Banu, C. Maier, C. Teodosiu, *Int. J. Plast.* **2006**, *22*, 2226.
 [49] C. Varvenne, O. Mackain, E. Clouet, *Acta Mater.* **2014**, *78*, 65.
 [50] J. F. March-Rico, G. Y. Huang, B. D. Wirth, *J. Nucl. Mater.* **2020**, *540*, 152339.
 [51] C. N. Tome, R. A. Lebensohn, U. K. Kocks, *Acta Mater.* **1991**, *39*, 2667.
 [52] A. Akhtar, *Acta Metall.* **1973**, *21*, 1.
 [53] F. Long, F. Xu, M. R. Daymond, *Metall. Mater. Trans. A* **2013**, *44*, 183.
 [54] L. Saintoyant, L. Legrasa, Y. Brechet, *Scr. Mater.* **2011**, *64*, 418.
 [55] M. H. Li, M. Ma, W. C. Liu, F. Q. Yang, *J. Nucl. Mater.* **2013**, *433*, 6.
 [56] K. Y. Zhu, D. Chaubet, B. Bacroix, F. Brisset, *Acta Mater.* **2005**, *53*, 5131.
 [57] M. Jedrychowski, B. Bacroix, O. U. Salman, J. Tarasiuk, S. Wronski, in *36th Riso Int. Symp. on Materials Science* **2015**.